Ultrasonically stimulated thermography for crack detection of turbine blades

Frank Mevissen and Michele Meo

Materials Research Centre, Department of Mechanical Engineering,

University of Bath, Bath, BA2 7AY, UK

E-mail: f.mevissen@bath.ac.uk,

Correspondence: m.meo@bath.ac.uk

Abstract

The hot gas components in a gas turbine have to withstand extreme loads. As failure of turbine blades could have catastrophic consequences, the integrity of the entire engine must always be guaranteed, hence quick and reliable structural health monitoring (SHM) or nondestructive testing techniques (NDT) are essential.

In this work, an ultrasonic stimulated thermographic test system was developed to efficiently detect cracks in turbine blades. The used technique is based on the ultrasound excitation with a piezo actuator, where the contact surfaces of the crack are excited and generate frictional heat which is captured by a thermal imaging camera. A method was developed, where the temperature increase is measured as a function of the electrical energy supply to the actuator. This allows understanding crack topology and the prediction of preloads in the crack. Numerical analysis were conducted for optimising the frequency to be excited for the type of damage experienced by the blade and for understanding the basic physics of the coupling between cracks configuration, local crack velocity and temperature increase. The procedure presented helps to efficiently detect cracks and to optimize the inspection cycles of these components.

Keywords: Infrared thermography; Vibrothermography; Crack detection; Gas turbines

1 Introduction

Different causes can lead to failure of components in a gas turbine [1]. Among various NDT methods for damage imaging, the vibro-stimulated thermography process has been developed in recent years to detect cracks quickly and efficiently. A component is vibrated so that the surfaces of the crack rub against each other and the generated frictional heat can be detected using a thermal imaging camera.

There are different possibilities how infrared thermography can be used for NDT [2–4]. Rahammer et al. conducted vibrothermal tests in composites using local defect resonance (LDR) technology [5] to investigate the changed resonance behaviour due to the changed stiffness in the area of the crack. Vibrothermography successfully demonstrated the viscoelastic temperature increase due to the delamination of composites [6, 7], while Solodov et al. utilised Chladni figures to demonstrate and visually illustrate resonance defects [8]. Gao et al. used statistical methods to detect cracks in turbine blades using sonic IR [9], and Obeidat et al. developed algorithms for post-processing to better extract damages [10–12]. The effect on the temperature of a closing crack was studied by Lu et al. [13], and the energy and heat index was developed for crack classification [14–16] based on the dissipated energy in the crack. Rothenfusser et al. examined the behaviour of open and closed cracks in turbine blades in an energy context [17]. Mendioroz et al. developed a technique to detect vertical cracks with a thermal imaging camera using ultrasound excitation [18]. Cracks in aluminium structures were successfully detected using sonic IR thermography and extended post-processing techniques to process the results [19]. Weekes et al. successfully detected cracks under a ceramic thermal barrier coating (TBC) used in many hot gas components in gas turbines [20], and Zang et al. developed finite element methods for verifying experiments using sonic IR on turbine blades with cracks [21, 22].

In the literature overview shown so far, single frequencies were used for excitation. Studies with multi-frequency excitations are presented in the following.

Zang et al. excited turbine blades using multiple frequencies to locate cracks with a thermal imaging camera [23, 24], and some studies used high-frequency loudspeakers as a source of excitation [25, 26]. Kang et al. increased the vibration amplitudes in the test component through an alternative constructive fastening solution for the ultrasonic horn and test component [27]. It was shown that different excitation frequencies offers advantages in crack detection. Holland successfully detected delamination under the TBC of turbine vanes

with a broadband vibrothermography technique [28]. A frequency dependency of the heat generated at the flaws was shown.

Many technical possibilities can stimulate and vibrate the components, such as using sonotrodes [29–45], where 20 to 40 kHz signals are transmitted with high energy to the component to be measured. This creates a quasi-chaotic excitation, since single impulses are mainly transmitted and no periodic signals [18, 20, 34, 38, 43, 45–48]. A disadvantage is that damage to the contact surface of the sonotrode with the test component can occur [31, 33, 38, 44]. Typical piezoelectric sensors can also be used for excitation [49–51]. Dyrwal, Meo and Ciampa used air-coupled transducers (ACT) to excite turbine blades to detect cracks with thermography [52]. An advantage here is the contactless use of these transducers, but the whole system sensitively reacts to the position of the sensor and to smallest deviations of the focusing point.

The aim of this work was the development of an efficient detection and classification of cracks with an ultrasonic stimulated thermal wave imaging approach. In addition, a novel developed procedure was used to identify preloads in cracks. This is an important indicator of plastic deformations caused by one of the typical failure modes in turbine blades. A piezo actuator was used as a source of excitation in this study, which allowed exciting the test components with frequencies up to 100 kHz and detecting the generated frictional heat using a thermal imaging camera. The turbine blades were excited indirectly via a rigid holding device to prevent damages to the blades and the TBC. For this purpose, turbine blades were used with cracks located at different positions on the trailing edges. This cracks formed during operation in a gas turbine.

The temperature increase on the cracks was mapped as a function of the excitation frequencies. This was used to investigate the crack behaviour using varying actuator amplitudes with constant excitation frequencies. Finite element simulations were developed to study the behaviour of the crack and to optimise the experimental approaches. It was numerically demonstrated the importance of exciting the appropriate velocity component to generate frictional heat when the crack is open or closed. The generated heat was calculated numerically and compared with the experiments.

2 Specimen description

For the thermographic study, 12 turbine blades made from Inconel 628 of a 10 MW industrial gas turbine with cracks at the trailing edges were used. These blades are internally cooled. The cooling air is led into the blade via the blade root and exits after serpentine

cooling via different exit slots at the trailing edge. Figure 1 shows the positions of the cracks on the trailing edges of the turbine blades for further evaluations. In Table 1, all blades were summarised with corresponding names, crack positions and the visible crack lengths.

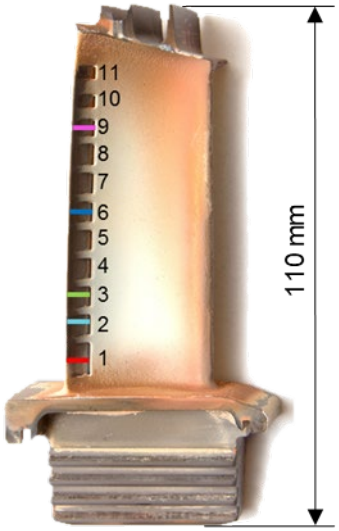

Figure 1. Cracked turbine blades.

Table 1. Investigated turbine blades – overview.

Blade name	Crack in cooling air chamber	Visible Crack length L [mm]
B327	1	1.6
B285	1	4.5
B100	2	5.4
B046	2	6
B189	2	6
B154	2	6.1
B221	2	6.6
B259	3	2.4
B115	3	5.8
B254	3	6.8
VKH1084	6	2.5
B286	6	6.1
B189	9	-

3 Experimental setup

A piezo actuator was used to vibrate the turbine blades. Typical applied strains are 0.1% to 0.15% of the actuator length. Piezo actuators behave like capacitive loads, which is why their charging and discharging currents increase with the working frequency. The preloaded actuator from Piezosystem Jena was used due to its robust design and low heat impact area. Table 2 summarises the properties.

Table 2. Properties – piezo actuator.

Type	Dimensions [mm]	Stiffness [N/µm]	Displacement [µm]	Mechanical resonance [kHz]	Blocking Force [N]
Piezosystem Jena PiSha 150/16/2	Ø25×29 Holder: Ø10×4	600	2	40	1000

The entire scheme of the experimental setup is shown in Figure 2(a). The actuator was directly bolted to the mounting device of the turbine blade using internal thread (Figure 2(b)).

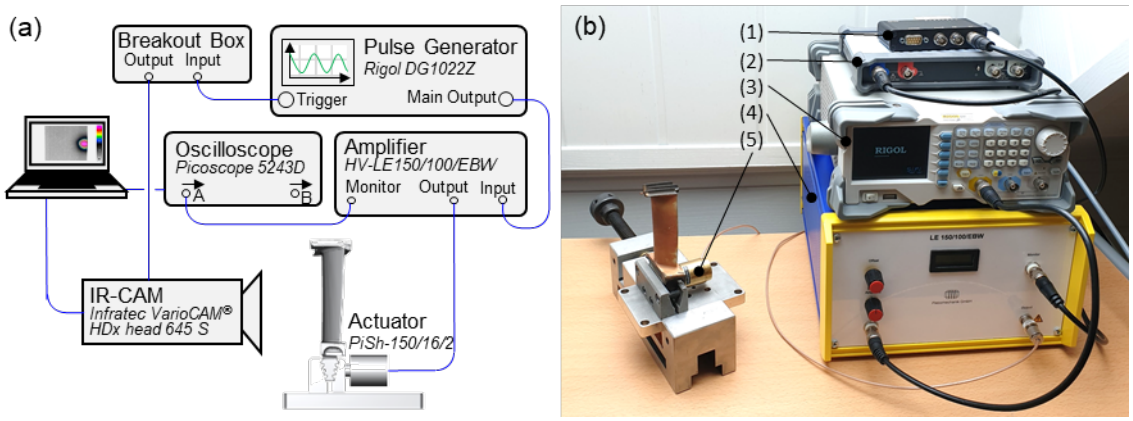

Figure 2. Experimental setup: (a) Scheme; (b) Components: (1) Breakout box, (2) Oscilloscope - Picoscope 5243D, (3) Puls generator - Rigol DG1022Z, (4) Amplifier - HV-LE150/100/EBW, (5) Piezo actuator - PiSha150/16/2.

A linearly rising sine wave signal generated by the Rigol DG1022Z pulse generator was used to excite the crack resonance frequencies. This signal is amplified by the device HV-LE150/100/EBW from Piezosystem Jena. The extended bandwidth of the amplifier introduces sufficient power over a large frequency range to the piezo actuator. As a control, the signal was transmitted via the monitor output to an oscilloscope and further evaluated using a computer. A breakout box was integrated via the trigger output to synchronise the frequency signal of the pulse generator with the recorded images of the thermal camera. For recording, the Infratec thermography system was used with the VarioCAM® HDx head research 645S camera, which is an uncooled micro bolometer camera with a detector format of 640 × 480 pixels and automatic focusing. The noise equivalent differential temperature (NETD) is up to 20 mK.

The device for blade mounting was clamped to achieve maximum system rigidity, and to avoid erroneous reflection measurements, a black paper box was placed over the specimen.

4 Thermographic spectra

To examine the investigations with increasing energy supply in the actuator, the frequencies leading to the highest temperature increase were first determined. For this purpose, the thermograms for all turbine blades were measured.

All measurements were performed in 5 kHz steps and synchronised with the highest accuracy. The frequency was linearly increased by 60 seconds for each excitation block, which guaranteed detecting small temperature increases. This was performed in the frequency range of 0 to 100 kHz.

Thermal energy is also transferred into the system through the piezo actuator's heat and can thereby influence the result of the thermal imaging camera measurement. An influence of the heating of the ambient air and convective transmission to the blades was not measured. The thermal power P_{th} generated in the actuator can be estimated as follows [53] (Equation (1)):

$$P_{th} \approx \frac{\pi}{2} tan(\delta) f C U^2, \quad (1)$$

where $tan(\delta)$ is the dielectric loss factor (ratio of effective to reactive power), f the working frequency, C the actuator capacitance and U the voltage difference between positive and negative peak voltage. Figure 6(a) shows the heat loss, P_{th}, as a function of the input voltage, U, for frequencies up to 100 kHz. The frequency influences the thermal output emitted, where the higher the actuator frequency, the greater the temperature increase.

Measurements from 0 to 100 kHz were performed to estimate the heat influence on the experimental setup (Figure 6(b)). Temperature profiles were measured at different positions and compared regarding the outer shell of the actuator (1), the contact surface for the washer (2), the holder (3), the inner shroud of the turbine blade (4) and two positions on the airfoil (5) and (6). The temperature significantly rises at the contact surface (2) with an excitation of 10 kHz, and a temperature increase of 4.2 K was measured at 30 kHz to 40 kHz.

This also affects the airfoil, where the temperature begins to rise continuously from an excitation of 20 kHz. The influence on two cooling air outlets on the airfoil were also evaluated. A maximum temperature increase of 1.19 K was measured at the position of the first cooling air chamber (5), further up on the ninth cooling air chamber (6) a maximum of 1.03 K.

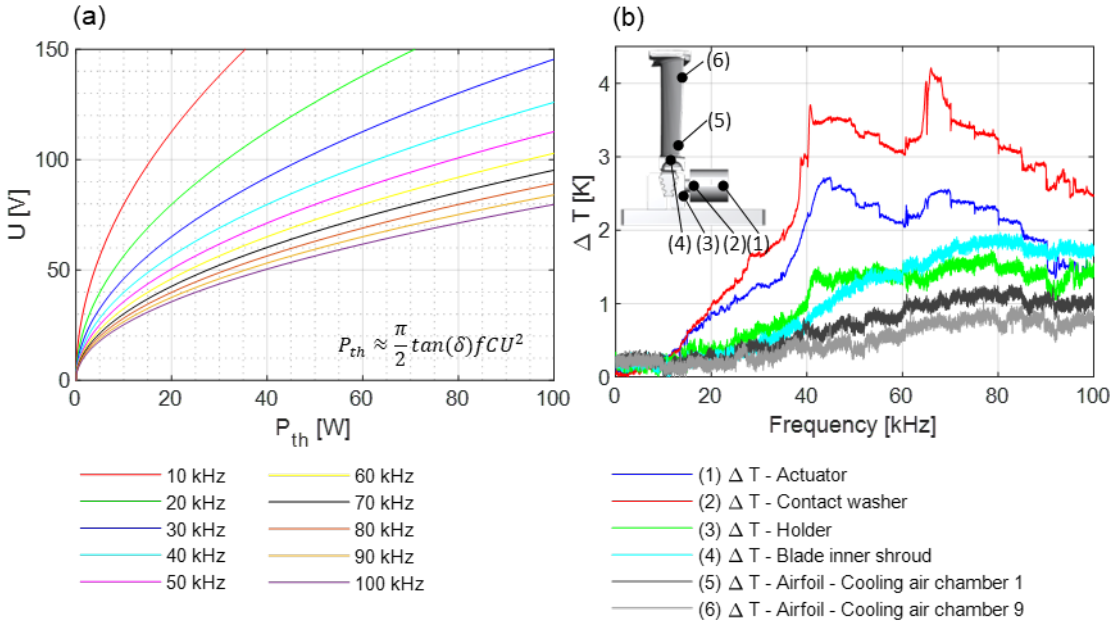

Figure 3. Temperature influence actuator: (a) Theoretical heat loss actuator - U f(P_{th}); (b) Experimentally determined heat transfer.

The theoretical calculations and experiments showed actuator influence on the heating of the turbine blade with a slow transfer of heat to the test object. Rapid heating in the crack area due to friction represents a clear difference detectable due to the higher temperatures.

Figure 4 shows the thermograms of the various turbine blades and cooling air openings. The designations C1, C2, C3, C6 and C9 in the figures describe the evaluated positions of the cracks on the turbine blades. The significant temperature increases occur primarily in the frequency range from 30 to 50 kHz for all measurements. As already shown in Figure 3(b), the general temperature difference increases continuously. Nevertheless, the temperature peaks were clearly identified. With consideration of all blades, the arithmetic average temperature increase was 6.5 K. In the case of cracks in the sixth chamber, the frequencies also shift to higher values since a maximum temperature increase of 26 K was measured (Figure 4-C6(b)). These significant increases in temperature are certainly favoured by the rigid clamping and thus by the direct transmission of the actuator energy.

The crack in the ninth chamber (Figure 4-C9(a)) is noteworthy, as a crack in the second chamber was originally detected on blade B189, but a further crack was not detected using conventional inspection methods and only made visible by thermographic experiments. This crack was located under the TBC.

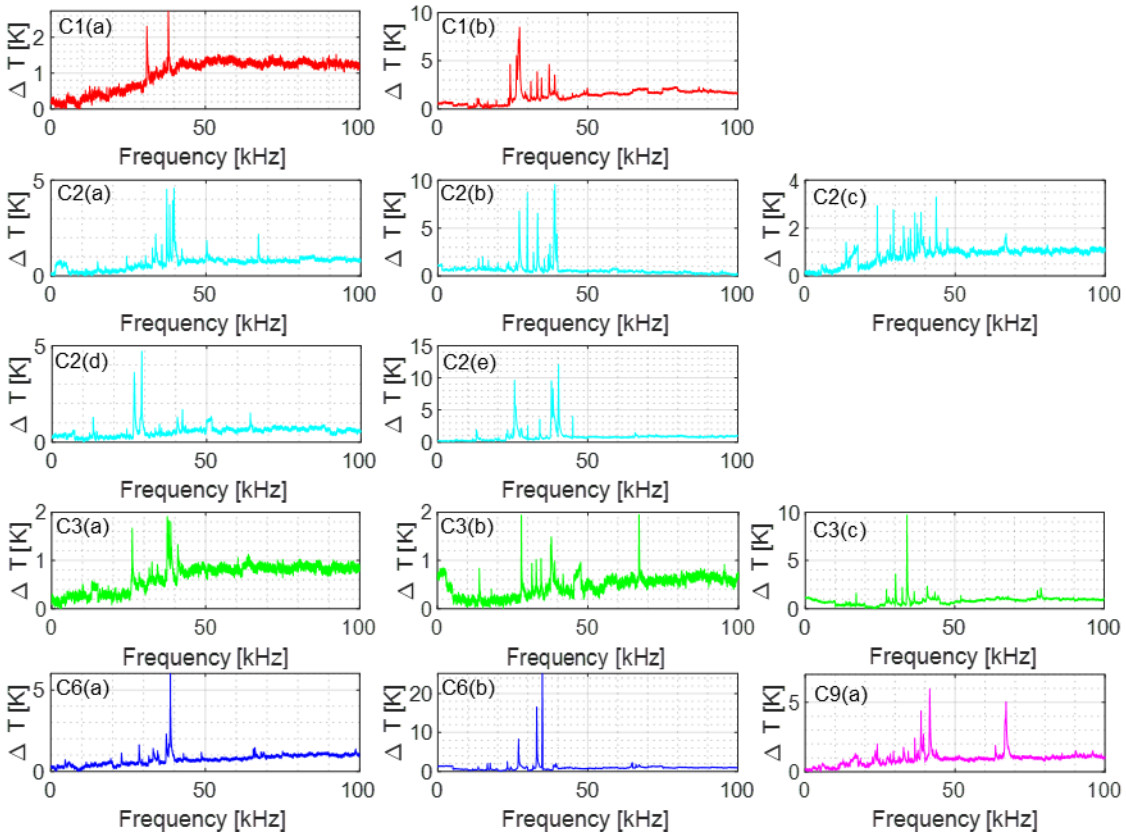

Figure 4. Thermograms: C1(a) B327; C1(b) B285; C2(a) B100; C2(b) B046; C2(c) B189; C2(d); C2(e) B221; C3(a) B259; C3(b) B115; C3 (c) B254; C6(a) VKH1084; C6(b) B286; C9(a) B189.

Some cracks also showed two positions of high heat generation. The point of maximum heat generation of all blades, L1 (Figure 5), is approximately 50% of the visual crack length, which proves that the cracks are wedge shaped and slightly open to the outside. This also means that there are plastic deformations in the areas of the cracks or erosion. Since there are mainly turbine blades with cracks in the second chamber, these were dominant for the evaluation. In addition, for blade B254 the heat generation point was located very deep in the component (88% compared to the visual crack length, L).

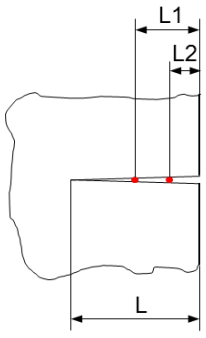

Figure 5. Positions heat generation.

Table 3 summarises the most important results of the experiments. The crack dimensions and positions (L1, L2) of the temperature generation are shown along with the highest temperature peaks with the corresponding frequencies. The number of measured peaks in the thermograms provides information about incorporating the thermographic measuring method.

Table 3. Results thermography turbine blades – summary.

Blade name	Crack chamber	Visible Crack length L [mm]	Position max. heat generation		Peak ΔT [K] [1]	Peak f [kHz] [1]	No. Peaks
			L1 [mm]	L2 [mm]			
B327	1	1.6	1.3	-	2.7	38.0	6
B285	1	4.5	3.6	2.3	8.48	27.25	22
B100	2	5.4	2.5	1.1	4.6	39.7	18
B046	2	6	1.9	-	9.6	39.0	16
B189	2	6	3.2	-	3.3	43.7	19
B154	2	6.1	4.7	1.0	4.7	29.0	11
B221	2	6.6	3.5	2.2	12.1	40.3	13
B259	3	2.4	1.1	-	1.9	37.5	11
B115	3	5.8		-	2.0	67.0	11
B254	3	6.8	6.6	2.2	9.7	34.0	14
B286	6	6.1	2.7	0.9	25.2	34.8	14
VKH1084	6	2.5	0.9	-	6.0	38.7	18
B189	9	-	2.2	1.4	5.93	41.56	16

[1] Refers to max. heat generation point L1.

The frequencies determined from the maximum temperature peaks serve as the basis for the investigations in the next section.

5 Temperature behaviour with increasing energy supply

In the previous section, the frequency was gradually increased and relevant crack resonance frequencies determined using thermography. Next, the frequencies with the highest temperature increase were kept constant for the individual blades while the energy supply to the actuator (amplitude) was gradually increased. The electrical power is defined as [53] (Equation (2)):

$$P_{el} = \frac{1}{2} C U^2 f. \tag{2}$$

Figure 6 show the temperature behaviour with slowly rising electrical energy in the piezo actuator. The frequencies with the highest temperature increase (Table 3) were selected for the individual blades and kept constant for the studies. After each measuring point, the actuator was switched off for electrical voltage readjustment. The actuator was activated for 2 seconds at each measuring point. This concept also works with frequencies with a lower temperature increase, but the frequencies with the peak temperatures offer the best possible response to even small actuator excitations.

The power display on the abscissa was shown in a standardised manner (P_{norm}) since the induced power in the actuator fluctuates depending on the excitation frequency.

The closer the friction point is to the trailing edges of the blades, the higher the relative sliding speeds and thus also the temperature. Uncertainties occur such as residual internal stresses or constraints due to the crack topography. The curves are characterised by different curve gradients. If the curve gradient is negative, saturation occurs and the temperature increase is limited, which could indicate closed cracks. With positive gradients, the temperature continues to rise and it is assumed that the crack has minimal inner constraints.

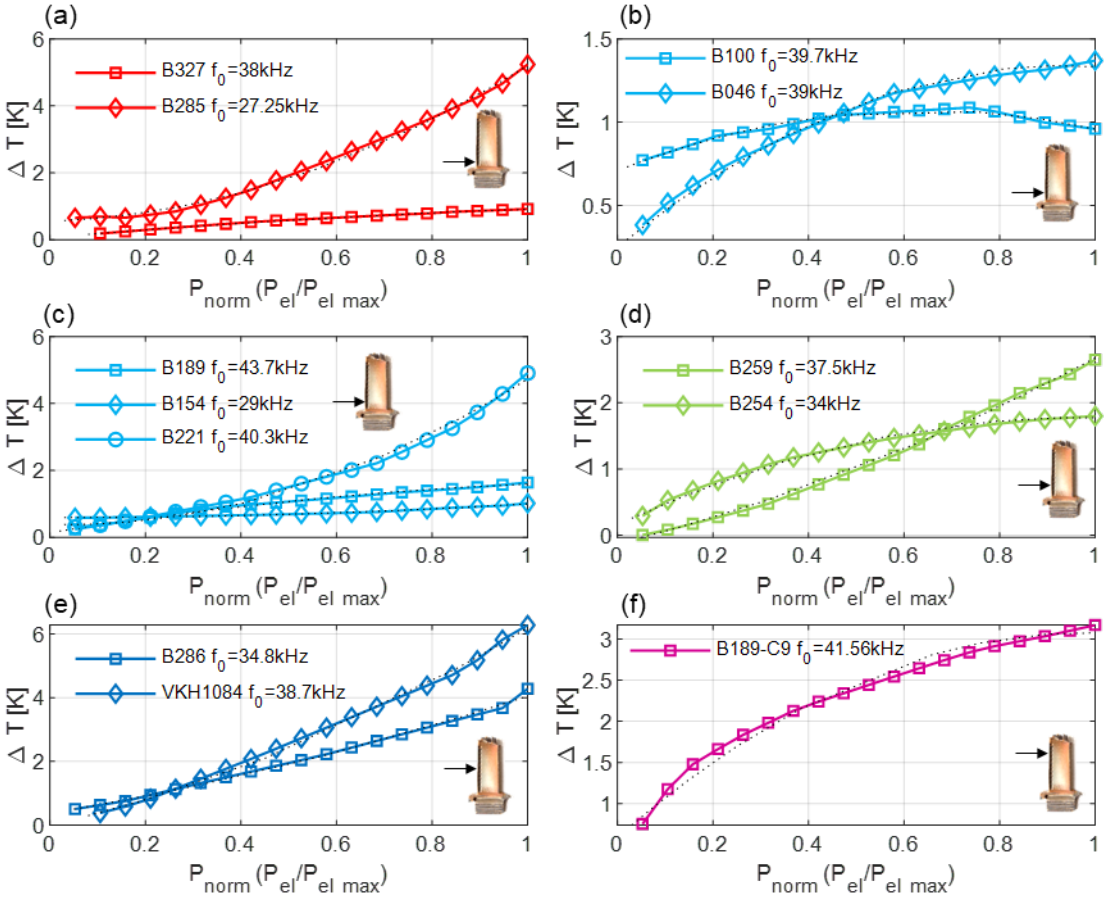

Figure 6. Heating behaviour: (a) Chamber 1; (b, c) Chamber 2; (d) Chamber 3; (e) Chamber 6; (f) Chamber 9.

A quadratic fitting curve was used through the measuring points on all measurements (dotted line). It can be observed that there is a direct connection to the kinetic energy ($E_{kin} = \frac{1}{2} m \vec{v}_{sl}^2$) since the measured temperature is proportional to the relative sliding velocity ($\Delta T \propto \vec{v}_{sl}$). If excitation occurs in the resonance area of the crack, a significant part of the energy induced in the actuator was converted into crack vibration.

6 Preload

Different behaviour of the cracks were determined, where constraints from preload forces were assumed. Therefore, the influence of preloads on the cracks was examined more closely. Figure 7 shows an experimental setup to demonstrate a preload's influence on thermographic examinations. A metallic body is clamped in the test setup and was painted matte black to avoid reflections. Using additive manufacturing, a device was constructed to guide a cylindrical pin, which should lead to a heat increase on the friction surface of the device. To measure the temperatures with changed preloads, the cylinder pin is preloaded with a compression spring and grub screw. The influence of the screwed-in threaded pin on the inertia of the vibrating system is estimated to be negligible. Six different load positions were examined (0.14 N to 0.98 N).

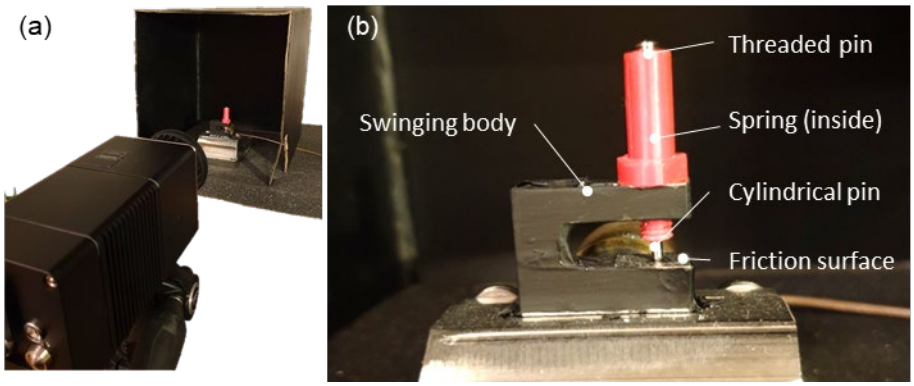

Figure 7. Influence preload: (a) Experimental setup - overview; (b) Experimental setup - components.

Figure 8 shows the result, where the input energy, P_{el}, was illustrated standardised. With small contact forces, a convex course appears, which becomes concave with higher forces. Quadratic behaviour occurs, as demonstrated in the other experiments. The numerical evidence and comparison are shown in Section 7.3.

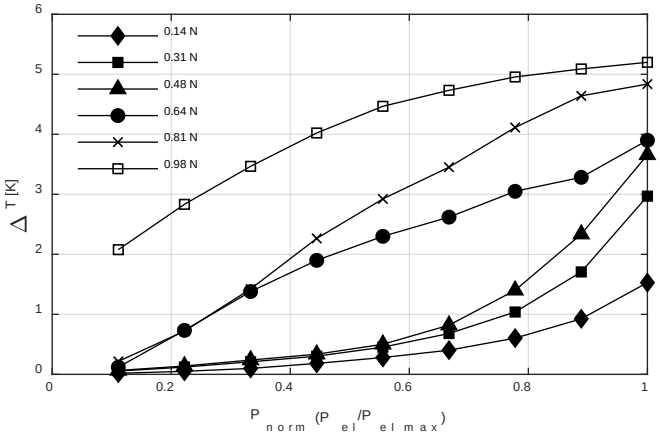

Figure 8. Experimental evidence influence preload.

7 FEM Simulations

Cracks react differently to different excitation frequencies or excited wave modes. Using the finite element method (FEM), the excitation frequency could be optimised to achieve the highest temperature increase at crack locations. The different velocity vectors in the crack area were calculated and compared with the simulated temperature increases due to friction. Figure 8 experimentally showed a preload's influence on the thermographic results, which were numerically evaluated and compared.

7.1 FEM Model

The blade model was geometrically simplified for the numerical thermographic simulations. To avoid influencing the thermal flow and stiffness, the FEM model's internal cooling channels were modelled. The lower surface was fixed, and the periodic excitation, equivalent to the experiments, occurs over the root area of the blade (Figure 9). This excitation is transferred to the crack model and vibrates this region. A sufficiently small time increment must be selected to correctly represent the temperature increase ($6e^{-5}$ s). With the Ansys calculation program, the "CoupledFields" extension is required to calculate temperature increases due to friction. The thermo-mechanical contact condition was programmed via the Ansys Parametric Design Language (APDL). The crack was simulated using a frictional contact algorithm, and an initial force of 10 N was applied whereby the contact areas were lightly pressed together.

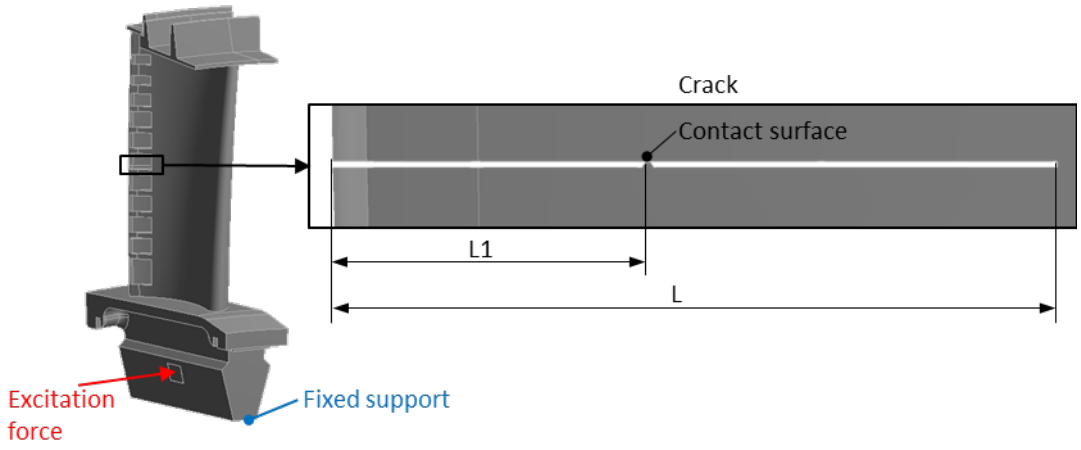

Figure 9. Thermographic FEM model.

The crack was modelled over the visual crack length, L, and the heat generation point, L1, where the temperature-increase evaluation was conducted. The surfaces to the right and left of the heat generation zone move freely and cannot overlap during vibration.

The damping of the entire system significantly influences the measured results. Many factors have influence which cannot be mapped with FEM due to the chosen system boundary. The ground below the measuring device also affects the damping. One method is to experimentally determine the attenuation for the numerical simulations. The Rayleigh damping $\boldsymbol{C} = \alpha_{D1}\boldsymbol{M} + \alpha_{D2}\boldsymbol{K}$ is used for this purpose, where α_{D1} is the proportionality constant of the mass matrix and α_{D2} the proportionality constant of the stiffness matrix. High-frequency vibrations are damped by the factor α_{D2} and low-frequency vibrations by the factor α_{D1}. If the damping ratios of two different vibrations are known (λ_{Di}), these factors can be calculated with Equation (3):

$$\alpha_{D1} = \frac{2\omega_1\omega_2}{\omega_2^2-\omega_1^2}(\lambda_{D1}\omega_2 - \lambda_{D2}\omega_{D1}),$$
$$\alpha_{D2} = \frac{2(\lambda_{D2}\omega_2-\lambda_{D1}\omega_1)}{\omega_2^2-\omega_1^2}. \quad (3)$$

The experiment was positioned on the same ground as those in the previous section. The blade was manually excited and the vibration measured using a portable laser vibrometer (Polytec Laser PDV 100). These experiments were repeated with different samples. The decay coefficient, δ, is determined by the logarithmic decrement with the measured values $\delta_i = \frac{1}{n} ln \frac{x_D(t)}{x_D(t+nT_D)}$, where n is the number of measured oscillations, t is the time, T_D are the periods and x_D are the vibration amplitudes of the decaying vibration. The value i describes the respective evaluated frequency. The damping ratio $\zeta_i = \frac{1}{\sqrt{1+(\frac{2\pi}{\delta_i})^2}}$ was then determined. The λ_D values are the values of ζ, which are given as percentages, which were used to calculate the damping factors of α_{D1} and α_{D2} for the FEM calculation (Table 4).

Table 4. Experimental determined damping values.

f_1 [Hz]	δ_1 [s^{-1}]	ζ_1 [%]	f_2 [Hz]	δ_2 [s^{-1}]	ζ_2 [%]	α_{D1}	α_{D2}
3263	7,1	0,035	6707	11,53	0,027	11,74	$6{,}2e^{-9}$

7.2 **Crack dynamics**

In this section, the different crack modes are shown, the velocity vectors are computed and the reaction forces of the cracks' contact surfaces are demonstrated for comparison.

If a component with an outwardly open crack is set in oscillation, different vibration modes result depending on the resonance frequency at the crack region (Figure 10). The local resonance crack modes can be exploited to generate a high temperature gradient.

The behaviour of the rubbing mode in y-direction can be compared to that of a mass-swinging pendulum (Figure 10(a)), where due to laws of energy conservation, the kinetic

energy is equal to the potential energy. In the maximum deflection at point P1, the oscillation speed and thus also the kinetic energy are zero and the potential energy in this case is the strain energy with the maximum value $E_{pot} = E_{strain} = \frac{1}{2}VE\varepsilon^2$. When swinging back to point P2, the strain energy is zero and the kinetic energy also reaches its maximum by the maximum swinging speed $E_{kin,y} = \frac{1}{2}m\dot{y}^2$ in the y-direction. The sliding velocity at the contact point of the crack thus leads to an increase in temperature, which is important for thermographic measurements.

Figure 10(b) shows the shear vibration mode, where the energy behaviour is identical to the previous mode. This means that at P2 the kinetic energy reaches its maximum value ($E_{kin,x} = \frac{1}{2}m\dot{x}^2$), whereas in P1 the strain energy is maximum and the kinetic energy is zero.

The clapping mode, shown in Figure 10(c), allows the crack surfaces to clap onto each other, where the maximum speed is reached before the cracks' surfaces meet ($E_{kin,z} = \frac{1}{2}m\dot{z}^2$). Real systems always involve a combination of all three modes.

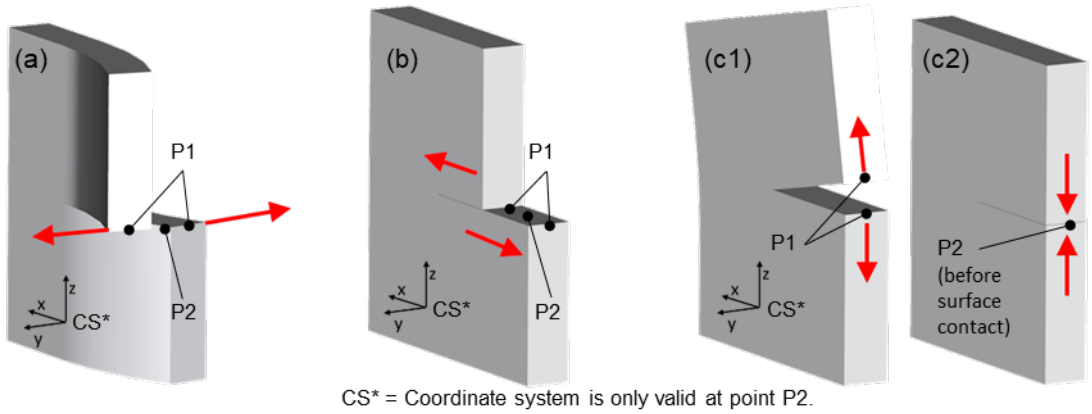

Figure 10. Crack modes: (a) Rubbing mode y-direction; (b) Rubbing mode x-direction; (c) Clapping mode z-direction.

The FEM investigations were conducted similarly to the experiments in the frequency range from 0 to 100 kHz (Section 4). The simulation results showed the behaviour of the various vibrating crack modes (Figure 10). Figure 11(a) and (b) show the velocity vectors and relative temperature increase due to friction for the exemplary B286 blade. The two temperature peaks (Figure 11(c)) occur at the points where the lateral velocity vectors have a maximum and the relative displacement creates a surface pressure at the crack location (Figure 11(b)). It was shown that the rubbing mode in y-direction (Figure 10 (a)) causes a large increase in measured temperatures.

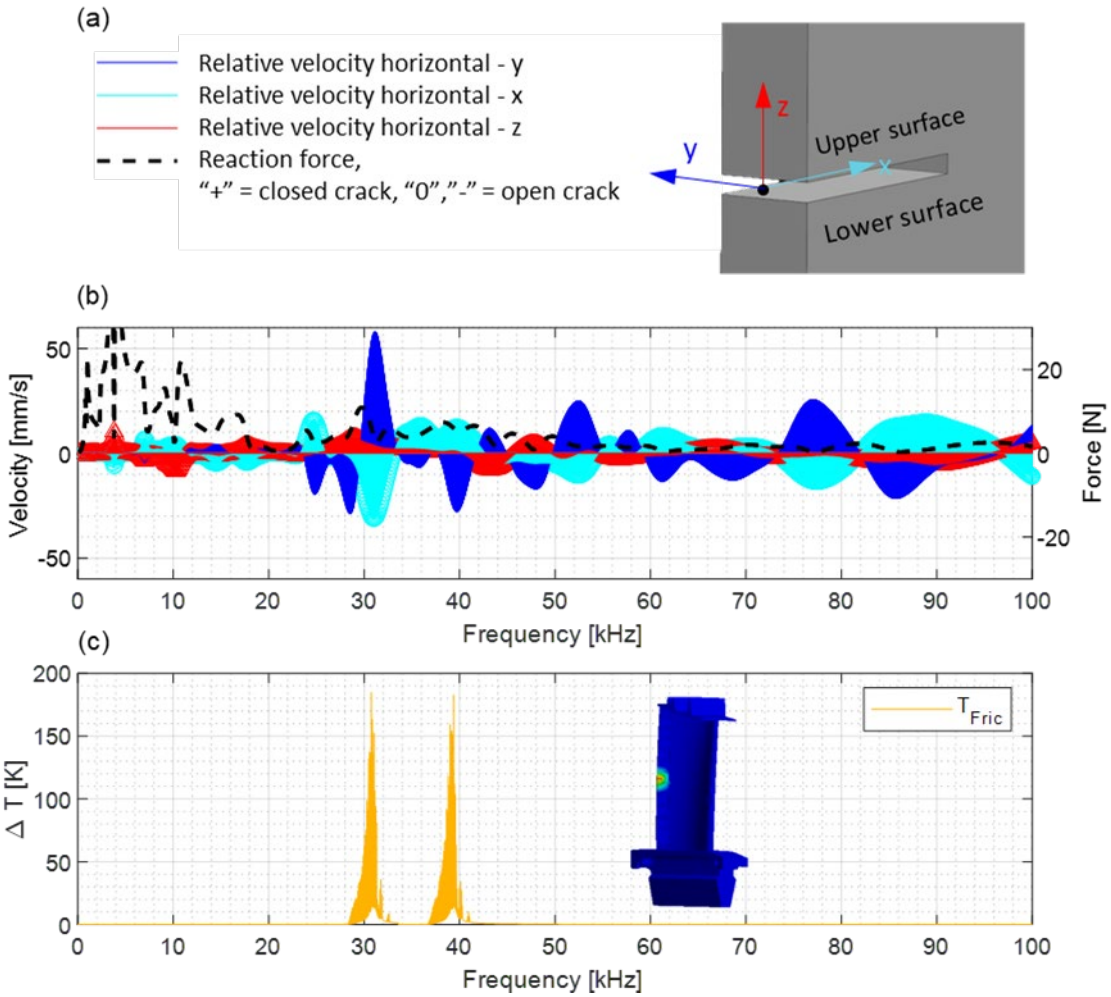

Figure 11. Results FEA: (a) Legend; (b) Crack velocity vectors and reaction forces; (c) Frictional temperature.

7.3 **Influence Preload**

A preload's influence on a crack during the thermographic experiments was examined for blade model shown in the previous section. The highest relative sliding velocity was determined at a frequency of 31.1 kHz (Figure 11(b)). Figure 12 shows the maximum temperature increase of the friction surface for the various contact loads from 10 N to 200 N. The preload was integrated into the surface normal of the upper contact surface of the model. The periodic sinusoidal excitation with a maximum amplitude of 1000 N was introduced into the test object to simulate the functionality of the piezo actuator.

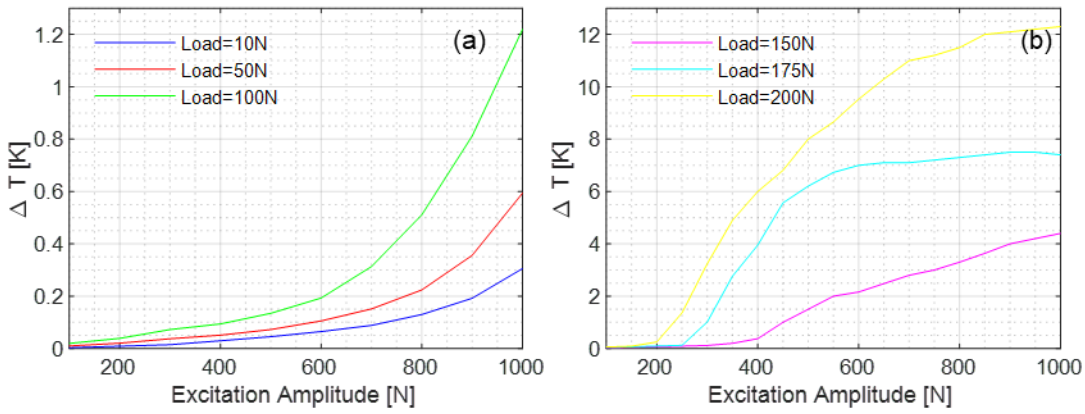

Figure 12. Study preload: (a) Load = 10 N to 100 N; (b) Load = 150 N to 200 N.

Figure 12(a) showed quadratic behaviour of the curves at forces from 10 N to 100 N, where if the load increases, the curve progressively reverses and becomes concave (Figure 12(b)). This confirms the previous assumption that the concave course of the curve evidences the presence of constraints due to vertical loads.

Figure 13 shows the qualitative comparison of the experimental data (Figure 8) and numerically determined data (Figure 12) for sequentially increased loads denoted by the increasing number of "+" signs.

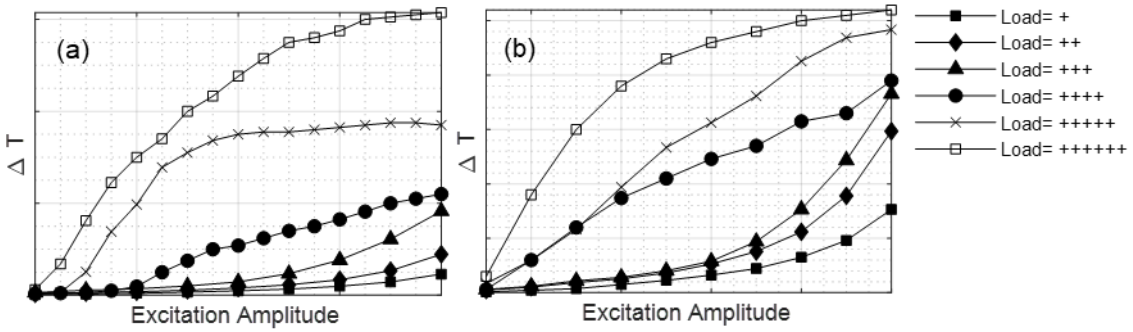

Figure 13. Comparison normalised preload study: (a) Numerical analysis; (b) Experimental results.

The verification of experiments and numerical calculations allow statements about possible preloads in cracks.

8 Conclusion

This paper proposes an ultrasonic stimulated thermal wave imaging system for crack detection in turbine blades. The presented method allows determining the presence of preloads on the crack surface as well as local plastic deformation. It was shown that the temperature increase as a function of the introduced actuator energy changes from concave

to convex with higher preloads in the crack areas. This was demonstrated by the development of finite element models able to reproduce results.

Turbine blades with real cracks on the trailing edges and in unknown locations under the ceramic TBC were investigated. The experimental results supported by finite element modelling results showed that the acquired thermograms provide crack detection and allow to provide information about the crack characteristic.

The presented procedure enables quick and accurate nondestructive investigation of turbine blades or other hot gas-leading components of gas turbines, leading to significant cost saving and safer operations.

Acknowledgement

The authors kindly acknowledge the financial support provided by the European Commission through the project TurboSens, grant agreement no. EFRE-0801016. In addition, thanks to the MAN Energy Solutions SE for their support.

References

1. Mevissen, F., & Meo, M. (2019). A Review of NDT/Structural Health Monitoring Techniques for Hot Gas Components in Gas Turbines. *Sensors, 19*(3), 711.
2. Maldague, X. P. (1993). *Nondestructive Evaluation of Materials by Infrared Thermography*. (1st edn). London: Springer London.
3. Ibarra-Castanedo, C., Tarpani, J. R., & Maldague, X. P. V. (2013). Nondestructive testing with thermography. *Eur. J. Phys., 34*(6), S91-S109.
4. Ciampa, F., Mahmoodi, P., Pinto, F., & Meo, M. (2018). Recent Advances in Active Infrared Thermography for Non-Destructive Testing of Aerospace Components. *Sensors, 18*(2), 609.
5. Rahammer, M., Solodov, I., Bisle, W., Scherling, D., & Kreutzbruck, M. (2016). Thermosonic Testing with Phase Matched Guided Wave Excitation. *J. Nondestruct. Eval., 35*(3), 154.
6. Renshaw, J., Chen, J. C., Holland, S. D., & Bruce Thompson, R. (2011). The sources of heat generation in vibrothermography. *NDT E Int., 44*(8), 736–739.
7. Renshaw, J., Holland, S. D., & Barnard, D. J. (2009). Viscous material-filled synthetic defects for vibrothermography. *NDT E Int., 42*(8), 753–756.
8. Solodov, I., Derusova, D., & Rahammer, M. (2015). Thermosonic Chladni figures for defect-selective imaging. *Ultrasonics, 60*, 1–5.
9. Gao, C., Mayton, D., Meeker, W. Q., Thompson, D. O., & Chimenti, D. E. (2007). Detecting cracks in fan blades using sonic IR. In *Review of Progress in Quantitative Nondestructive Evaluation: 34th Annual Review of Progress in Quantitative Nondestructive Evaluation, Golden (Colorado), 22–27 July 2007*. (pp. 1708–1715): AIP.
10. Obeidat, O., Yu, Q., & Han, X. (2016). Developing Algorithms to Improve Defect Extraction and Suppressing Undesired Heat Patterns in Sonic IR Images. *Sensing and Imaging, 17*(1), 2418.
11. Obeidat, O., Yu, Q., & Han, X. Develop algorithms to improve detectability of defects in Sonic IR imaging NDE. In *Review of Progress in Quantitative Nondestructive Evaluation*. (p. 100009).

12. Obeidat, O., Yu, Q., & Han, X. Further development of image processing algorithms to improve detectability of defects in Sonic IR NDE. In *43rd annual Review of Progress in Quantitative Nondestructive Evaluation*. (Vol. 36, p. 100007).

13. Lu, J., Han, X., Newaz, G., Favro, L. D., & Thomas, R. L. (2007). Study of the effect of crack closure in Sonic Infrared Imaging. *Nondestruct. Test. Evaluation, 22*(2-3), 127–135.

14. Morbidini, M. (2007). *A comparison of the vibration-modulation and thermosonic*. Ph.D Thesis. Imperial College London, London, UK.

15. Morbidini, M., & Cawley, P. (2008). The Reliable Implementation of Thermosonics NDT. In *17th World Conference on Nondestructive Testing, Shanghai, China, 25-28 October 2008*. (1st ed., 536, Vol. 975): AIP Conference Proceedings.

16. Morbidini, M., & Cawley, P. (2009). The detectability of cracks using sonic IR. *J. Appl. Phys., 105*(9), 93530.

17. Rothenfusser, M. (2004). Acoustic Thermography: Vibrational Modes of Cracks and the Mechanism of Heat Generation. In *Review of Progress in Quantitative Nondestructive Evaluation, Golden, Colorado (USA), 25-30 July 2004*. (pp. 624–631): AIP.

18. Mendioroz, A., Celorrio, R., & Salazar, A. (2017). Ultrasound excited thermography: an efficient tool for the characterization of vertical cracks. *Meas. Sci. Technol., 28*(11), 112001.

19. Guo, X., & Vavilov, V. (2013). Crack detection in aluminum parts by using ultrasound-excited infrared thermography. *Infrared Phys. Technol., 61*, 149–156.

20. Weekes, B., Cawley, P., Almond, D. P., Thompson, D. O., & Chimenti, D. E. The Effects of Crack Opening and Coatings on the Detection Capability of Thermosonics. In *Review of Progress in Quantitative Nondestructive Evaluation*. (30ab, pp. 399–406).

21. Zhang, D., Han, X., Newaz, G., Favro, L. D., & Thomas, R. L. (2013). Improvements on FEA with a two-step simulation of experimental procedures in turbine blade crack detection in sonic IR NDE. *AIP Conference Proceedings, 1511*, 518.

22. Zhang, D., Han, X., Newaz, G., Favro, L. D., & Thomas, R. L. (2012). Modeling turbine blade crack detection in sonic IR imaging with a method of creating flat crack surface in finite element analysis. *AIP Conference Proceedings, 1430*, 527.

23. Zhang, D., Han, X., & Newaz, G. Sonic IR crack detection of aircraft turbine engine blades with multi-frequency ultrasound excitations. In *Review of Progress in Quantitative Nondestructive Evaluation*. (pp. 1644–1651).

24. Zhang, D. (2014). *Study of Chaotic Ultrasound and Frequency Sweep Excitations in Sonic IR NDE Technology*. Ph.D. Thesis. Wayne State University, Detroit, MI, USA.

25. Zalameda, J. N., Winfree, W. P., Yost, W. T., Thompson, D. O., & Chimenti, D. E. (2007). Air coupled acoustic thermography (acat) inspection technique. In *Review of Progress in Quantitative Nondestructive Evaluation, Golden, Colorado, USA, 22–27 July 2007*. (pp. 467–474): AIP.

26. Solodov, I., Rahammer, M., Gulnizkij, N., & Kreutzbruck, M. (2016). Noncontact Sonic NDE and Defect Imaging Via Local Defect Resonance. *J. Nondestruct. Eval., 35*(3), 1–8.

27. Kang, B., Cawley, P., Thompson, D. O., & Chimenti, D. E. (2007). Multi-Mode Excitation System for Thermosonic Testing of Turbine Blades. In *Review of progress in quantitative Nondestructive Evaluation, Golden, Colorado, USA, 22–27 July 2007*. (pp. 520–527): AIP.

28. Holland, S. D. (2007). First Measurements from a New Broadband Vibrothermography Measurement System. In *Review of Progress in Quantitative Nondestructive Evaluation, Portland, Oregon, USA, 30 July-4 August 2007*. (pp. 478–483): AIP.

29. Pieczonka, L., Aymerich, F., Brozek, G., Szwedo, M., Staszewski, W. J., & Uhl, T. (2013). Modelling and numerical simulations of vibrothermography for impact damage detection in composites structures. *Struct. Control Health Monit., 20*(4), 626–638.

30. Polimeno, U., Almond, D. P., Weekes, B., & Chen, E. (2014). A compact thermosonic inspection system for the inspection of composites. *Composites Part B: Engineering, 59*, 67–73.

31. Homma, C. (2000). Study of the Heat Generation Mechanism in Acoustic Thermography. In *Quantitative Nondestructive Evaluation, Brunswick, Maine, USA, 31 July-5 August 2000*. (pp. 566–573): AIP.

32. Chen, J. C., Kephart, J., Lick, K., & Riddell, W. T. (2007). Crack growth induced by sonic IR inspection. *Nondestruct. Test. Evaluation*, *22*(2-3), 83–92.

33. Feng, F., Zhang, C., Min, Q., Zhu, J., Wang, W., & Chao, X. (2017). Heating characterization of the thickness-through fatigue crack in metal plate using sonic IR imaging. *NDT E Int.*, *87*, 38–43.

34. Han, X., Favro, L. D., & Thomas, R. L. (2011). Sonic IR Imaging of delaminations and disbonds in composites. *J. Phys. D Appl. Phys.*, *44*(3), 34013.

35. Han, X., & Song, Y. Study the effect of engagement force of ultrasound transducer on crack detectability in sonic IR imaging. In *Review of progess in quantitative Nondestructive Evaluation.* (Vol. 32, pp. 532–538).

36. Lick, K. E., Wong, C. H., & Chen, J. C. (2000). Determination of the Minimum Energy Required for Sonic-IR Detection. In *Review of progress in quantitative Nondestructive Evaluation, Portland, Oregon, USA, 30 July-4 August 2000*. (pp. 515–522): AIP.

37. Riddell, W. T., Chen, J. C., & Wong, C.-H. (2013). Effect of Fatigue Precracking on Crack Engagement during Sonic IR Testing. *Research in Nondestructive Evaluation*, *24*(1), 18–34.

38. Zhang, C., Feng, F., Min, Q., & Zhu, J. (2015). Effect of engagement force on vibration characteristics and frictional heating in sonic IR imaging. *NDT E Int.*, *76*, 52–60.

39. Zhang, D., Han, X., & Newaz, G. (2014). Sonic IR crack detection of aircraft turbine engine blades with multi-frequency ultrasound excitations. *AIP Conference Proceedings*, *1581*, 1644.

40. Chaki, S., Marical, P., Panier, S., Bourse, G., & Mouftiez, A. (2011). Interfacial defects detection in plasma-sprayed ceramic coating components using two stimulated infrared thermography techniques. *NDT E Int.*, *44*(6), 519–522.

41. Malfense Fierro, G. P., Ginzburg, D., Ciampa, F., & Meo, M. (2017). Imaging of Barely Visible Impact Damage on a Complex Composite Stiffened Panel Using a Nonlinear Ultrasound Stimulated Thermography Approach. *J. Nondestruct. Eval.*, *36*(4), 249.

42. Han, X. (2003). Frequency dependence of the thermosonic effect. *Review of Scientific Instruments*, *74*(1), 414–416.

43. Han, X., Zeng, Z., Li, W., Islam, M. S., Lu, J., Loggins, V., et al. (2004). Acoustic chaos for enhanced detectability of cracks by sonic infrared imaging. *J. Appl. Phys.*, *95*(7), 3792–3797.

44. Barden, T. J., Almond, D. P., Pickering, S. G., Morbidini, M., & Cawley, P. (2007). Detection of impact damage in CFRP composites by thermosonics. *Nondestruct. Test. Evaluation*, *22*(2-3), 71–82.

45. Kang B.B., Cho Y.H.,Baeg N.U., Na H.S. (2011). Characteristics of the Vibration Generated by Different Excitation Methods During Thermosonic Non-destructive Testing. In *9th world congress railway research 2011, Lille, France, 22-26 May.*

46. Han, X. (2004). Importance of Acoustic Chaos in Sonic IR Imaging NDE. In *Quantivative Nondestructive Evaluation.* (Vol. 700, pp. 496–500): AIP.

47. Riahi, M., Dehestani, P., & Valipour, A. (2016). Using finite element to estimate vibration energy loss by cracks in thermosonic phenomenon under chaotic and non-chaotic vibrations. *J. Vib. Control*, *22*(2), 457–467.

48. Abu-Nabah, B. A., & Al-Said, S. A. M. (2018). Sonic IR crack size estimation using 2D heat diffusion model with arbitrary heat source function along the crack. *Quant. Infrared Thermogr. J.*, *1*, 1–20.

49. Derusova, D. A., Vavilov, V. P., & Pawar, S. S. (2015). Evaluation of equivalent defect heat generation in carbon epoxy composite under powerful ultrasonic stimulation by using infrared thermography. *IOP Conf. Ser: Mater. Sci. Eng.*, *81*, 12084.

50. Parvasi, S. M., Xu, C., Kong, Q., & Song, G. (2016). Detection of multiple thin surface cracks using vibrothermography with low-power piezoceramic-based ultrasonic actuator—a numerical study with experimental verification. *Smart Mater. Struct.*, *25*(5), 55042.

51. Favro, L. D., Thomas, R. L., Han, X., Ouyang, Z., Newaz, G., & Gentile, D. (2001). Sonic infrared imaging of fatigue cracks. *Int. J. Fatigue, 23*, 471–476.

52. Dyrwal, A., Meo, M., & Ciampa, F. (2018). Nonlinear air-coupled thermosonics for fatigue micro-damage detection and localisation. *NDT E Int., 97*(3), 59–67.

53. Piezosytem Jena. Piezoline. https://www.piezosystem.de/fileadmin/redakteure/bilder/Sonstige/Piezofibel/Piezoline-piezosystem-jena.pdf. Accessed 27 October 2018.